

Instabilities in the wake of a circular disk

T. Bobinski,^{1,2} S. Goujon-Durand,² and J. E. Wesfreid²

¹Warsaw University of Technology, Institute of Aeronautics and Applied Mechanics, ul. Nowowiejska 24, 00-665 Warsaw, Poland

²Laboratoire de Physique et Mécanique des Milieux Hétérogènes (PMMH) [UMR 7636 Centre National de la Recherche Scientifique (CNRS)-École Supérieure de Physique et de Chimie Industrielles de la Ville de Paris (ESPCI)-Université Pierre et Marie Curie (UPMC)-Université Paris Diderot (UPD)], 10 rue Vauquelin, F-75005 Paris, France

(Received 18 March 2013; revised manuscript received 12 March 2014; published 23 May 2014)

Flow past a disk was investigated experimentally in a low-velocity water channel in the range of intermediate Reynolds numbers. Systematic experiments with flow visualization and particle image velocimetry measurements are presented. Different disks with the aspect ratio $\chi = d/h$ varying from 1 to 24 were investigated. The measurements were made in the range of Reynolds numbers from 0 to 500, where stationary and oscillatory instabilities appear. The influence of the aspect ratio on the value of onset instability, the evolution of perturbation, and the obtained vorticity bifurcation branches of the instability were identified.

DOI: [10.1103/PhysRevE.89.053021](https://doi.org/10.1103/PhysRevE.89.053021)

PACS number(s): 47.15.Fe, 47.15.Tr, 47.20.Ky, 47.32.ck

I. INTRODUCTION

Vortex shedding behind a general three-dimensional (3D) axisymmetric bluff body is an interesting research subject because it shows three-dimensional structures at the onset of instability. Similar behavior is seen behind spheres, disks, and bullets. These observations differ from vortex shedding behind very elongated bodies, e.g., transversal cylinders, for which coherent structures with spanwise vorticity appear at the onset. We note [1] that only few experiments exist for flow instabilities behind fixed disks normal to the flow [2–5]. Such instabilities have been mainly investigated numerically for disks of different thickness. Previous works distinguished at least four different flow regimes. The first regime has a steady axisymmetric base flow with a toroidal recirculation zone. After a first transition, the flow remains steady but the wake includes a pair of streamwise vortices. The second bifurcation forms a transition to the unsteady flow. Numerical simulations show different phenomena in this regime: Auguste *et al.* [6] observed vortices twisted around an axis of symmetry, Meliga *et al.* [7] observed shifted, double-sided hairpins, and Shenoy *et al.* [8] described 3D periodic flow with regular rotation of the separation region. The fourth regime, described similarly in all papers, constitutes an unsteady flow with regular hairpin shedding. To confirm these results and to increase our understanding of this interesting problem, it is crucial to investigate it experimentally. One of the main objectives of the present paper is to perform a full systematic study of the nonlinear evolution of the streamwise vorticity induced by the subsequent flow instabilities.

II. EXPERIMENTAL SETUP

The experiments were performed in a low-velocity water channel. The cross section of the channel was 10×10 cm. The diameter of the disk was $d = 1.2$ cm, which corresponds to a blockage ratio of 0.12 (disk diameter divided by channel width). Typical velocities were below 4 cm/s while the corresponding range of Reynolds numbers was between 50 and 500. The Reynolds number was defined as $\text{Re} = \frac{Ud}{\nu}$, where U stands for the free stream velocity normal to the disk and ν is the kinematic viscosity of water. The disk was supported

by a rigid bent tube mounted 10 cm in front of the disk. The cylindrical tube, with diameter of 0.2 cm, was hollow to allow injection of colorant. Six disks with thicknesses $h = 1.2, 0.9, 0.6, 0.4, 0.2,$ and 0.05 cm were investigated. To visualize the flow patterns, the laser-induced fluorescence (LIF) was used with fluorescein as a colorant. Measurements of the velocity field were made using a particle image velocimetry (PIV) system from LaVision®. The flow was seeded with spherical particles of a typical diameter of $11 \mu\text{m}$. The standard PIV employed in experiments involved a charge-coupled device (CCD) camera operating at 15 Hz, a double-pulsed YAG laser, a timer box for synchronizing the laser with the camera, and an optical module for producing the laser sheet.

Almost all PIV measurements were performed in the back-view configuration (laser sheet was perpendicular to the mean flow velocity) with an interrogation window of 32×32 pixels and an overlap of 50%. The distance between the two adjacent vectors in the plane of measurements was equal to about 0.8 mm.

The most important parameter in the present work is the longitudinal component of vorticity ω_z . Therefore, it is relevant to describe the measurement error of this quantity. One of the sources of uncertainty in PIV measurements is the velocity gradient. In case of the flow, investigated in this paper, velocity gradients are small as we are far from walls—the region of interest is in the middle of the channel (Lazar *et al.* [9]). As the transversal velocities of the flow are almost one order of magnitude lower than the longitudinal velocities, the number of the out-of-plane events is very small. The distortion of the view scene recorded by the camera lens, in the back view, is very weak as its influence is significant in the areas close to the edge of the image and spatially decreases towards the center of the image. This fact was taken into account, as the disk was placed in the center of captured images while the camera remained relatively far from the plane of measurement (1.1 m). As the main interest concerns the evolution of vorticity, another source of uncertainty has to be considered which is the truncation error associated with second-order finite difference scheme, in the estimation of vorticity (Lourenco *et al.* [10]). The velocity fluctuations, present in the obtained PIV velocity field, were randomly distributed in time with the standard deviation of $\delta v = 0.13$ mm/s. Taking into account spatial discretization

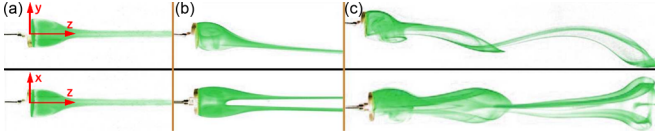


FIG. 1. (Color online) Visualization patterns (streaklines) for different flow regimes. Images at top and bottom are the side view and top view, respectively. (a) Steady axisymmetric flow ($Re = 50$). (b) Steady flow with planar symmetry ($Re = 135$). (c) Unsteady flow with hairpin shedding ($Re = 180$) for a disk with $d/h = 6$.

$\Delta x = 0.8$ mm one may determine the instantaneous vorticity error to be $\Delta\omega_z = 0.23$ s $^{-1}$.

III. EXPERIMENTAL RESULTS

A. Flow regimes

Three different flow regimes were distinguished experimentally for each disk (Fig. 1). The first is a steady axisymmetric flow with a toroidal recirculation zone behind the body. As the Reynolds number increases, the flow remains steady after a first transition, the toroidal recirculation zone distorts and becomes nonaxisymmetric while two longitudinal counter-rotating vortices are observed in the wake. With a subsequent increase in flow velocity, a second transition leads to unsteady flow with a regular hairpin shedding.

B. Onset values for different aspect ratios

To determine the onset values, the transversal velocity field was measured in a channel cross section to obtain the corresponding streamwise vorticity field. This measurement was possible because the end section of the channel has a transparent window perpendicular to the flow, which allows optical access without distortion. The longitudinal component of vorticity ω_z was measured in planes perpendicular to the mean flow velocity at different distances from the disk. The maximum value of vorticity was observed at a distance of $1.25d$ behind the disk (see Fig. 2).

The first bifurcation from the steady axisymmetric base flow ($\omega_z = 0$) to the steady planar symmetric flow with two counter-rotating vortices in the wake ($\omega_z \neq 0$) is illustrated

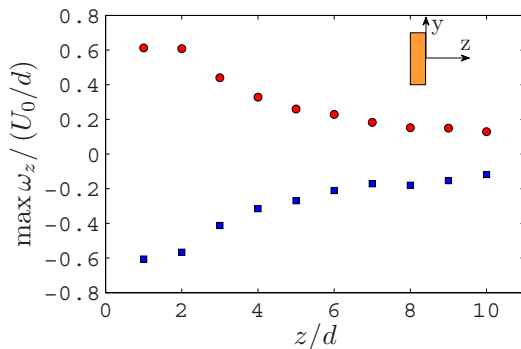


FIG. 2. (Color online) Maximum magnitude of longitudinal vorticity as a function of distance from the disk ($d/h = 2$, $Re = 221$). Blue squares correspond to negative vorticity (clockwise eddy). Red circles correspond to positive vorticity (anticlockwise eddy).

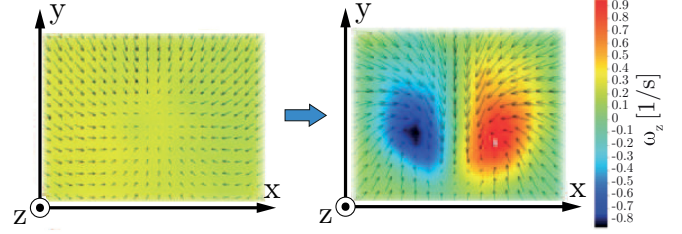


FIG. 3. (Color online) PIV images. (left) Steady axisymmetric flow ($d/h = 24$, $Re = 54$). (right) Steady asymmetric flow with two counter-rotating vortices ($d/h = 24$, $Re = 129$), obtained in a channel cross section at $z = 1.25d$.

in Fig. 3. The onset values of the steady instability Re_{c1} are presented for different disks, with different ratios of d/h in Table I as well as in Fig. 5, showing higher onset for thicker disks.

The subsequent second bifurcation leads to unsteady flow with periodic shedding in the form of hairpins. The time evolution of the obtained longitudinal vorticity field for this regime is shown in Fig. 4. The onset of unsteady instability is shown in Fig. 5 by circles. The onset dependence on Reynolds number is qualitatively similar as for the case of the first bifurcation.

For the thickest disks ($d/h = 1.33$ and $d/h = 1$), the first onset occurs for the highest Reynolds number, and in these cases it is possible to identify how the instabilities appear, first with small oscillations of the wake (values of onset given by triangles in Fig. 5) and later with hairpins. This is the same phenomenon described by Gumowski *et al.* [11] as “peristaltic oscillations.”

From the hydrodynamic point of view, increasing h provides more space to develop a thicker boundary layer. For the same Re value this implies lower shear strength U_0/δ and in consequence higher Re of the onset for the same regime of shear instability. This effect is strongly amplified by the opening of the streamlines behind a thicker body, which weaken the shear (Roshko [12]).

C. Effect of disk aspect ratio on magnitude of vorticity

The maximum magnitude of longitudinal vorticity $\max \omega_z$ was chosen as an order parameter for further investigation. This value was extracted from 100 frames of successive PIV measurements (which corresponds to nearly two cycles of oscillations in the unsteady regime). In the case of a steady regime with two counter-rotating vortices, the maximum

TABLE I. Onset values.

	Re_{c1}	$Re_{\text{peristaltic}}$	Re_{c2}
$d/h = 24$	108		146
$d/h = 6$	120		172
$d/h = 3$	142		202
$d/h = 2$	179		238
$d/h = 1.33$	218	305	317
$d/h = 1$	230	310	333

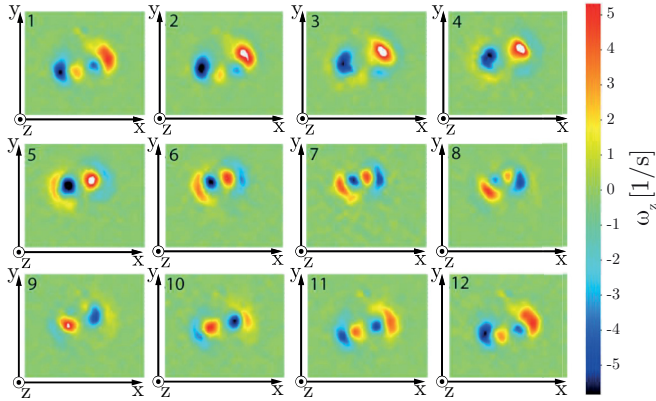


FIG. 4. (Color online) Vorticity fields for unsteady regime; one period of hairpin shedding ($d/h = 24$, $Re = 220$).

value of the vorticity component was determined from the averaged vorticity field. Thereby, the estimated relative error in this regime was less than 1%. In the unsteady regime, the maximum value of vorticity was searched in each frame. The average value of maxima present in the signal was taken as the more approximate contribution to the vorticity from the legs of the hairpins, parallel to the horizontal base flow. Two maximum values were determined for each snapshot, one corresponding to clockwise vorticity and the second corresponding to anticlockwise vorticity. The measurement error in this regime was estimated to be less than 5%.

Figure 6(a) shows typical bifurcation branches for a disk with $d/h = 3$. After the first bifurcation, the vorticity increases regularly in the regime with two steady counter-rotating vortices. After a second unsteady bifurcation, a significant change in the slope can be observed. This behavior was identified for different disk aspect ratios, as presented in Fig. 6(b). The behavior of maximum vorticity, by crossing the onset, seems to suggest a weak discontinuity. However, no systematic measurements were performed to identify the hysteresis of this phenomenon (by increasing and decreasing the Reynolds number). This weak jump may still result from inefficient resolution of the measurements. In the case of disks with $d/h = 1$ and $d/h = 1.33$, we did not observe a significant difference between the cases of steady flow with

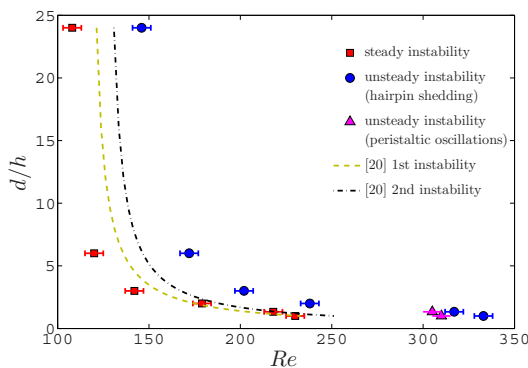


FIG. 5. (Color online) Onset values for different disks.

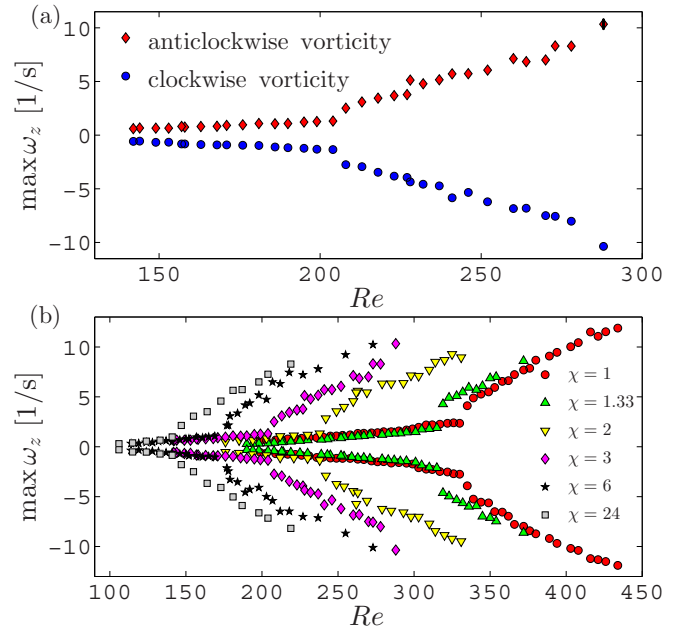


FIG. 6. (Color online) (a) Vorticity bifurcation branches for the disk with aspect ratio $d/h = 3$ (note the error bar for the typical measurement). (b) Vorticity magnitude for different disks.

planar symmetry and unsteady flow with hairpin shedding, corresponding to the peristaltic oscillations regime.

Returning to the stationary regime, we calculated the square of longitudinal vorticity (Fig. 7) and compared it with the predictions of a Landau model, where $\omega_z \sim (Re - Re_{c1})^{1/2}$, as discussed in the conclusions.

From the evolution of the maximum of ω_z^2 as a function of Re , we estimated the law of the nonlinear evolution as $\max \omega_z = g^{-1/2}[(Re - Re_{c1})/Re_{c1}]^{1/2}$, where g stands for the Landau constant, presented in Table II. We are aware that the disk support and the marginal inclination of the disk [13] introduce additional weak vorticity into the flow. However, following earlier results of Gumowski *et al.* [11], we expect that these perturbations are responsible only for fixing of the symmetry plane and producing the imperfect supercritical

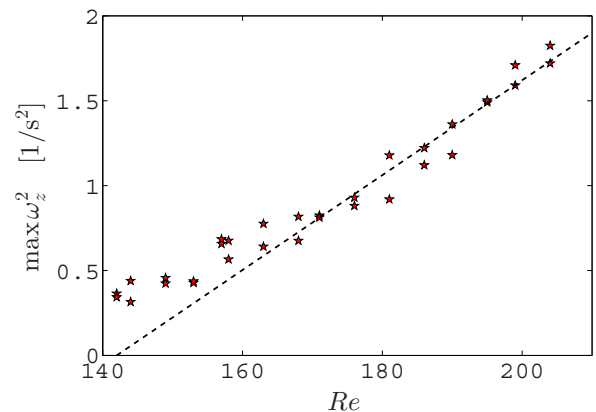


FIG. 7. (Color online) Square of maximum longitudinal vorticity for steady regime with two counter-rotating vortices for disk with $d/h = 3$ (broken line denotes the prediction of a Landau model).

TABLE II. Landau coefficients.

	g (first instability)	g (second instability)	$(c_0 - c_2)/(2\Pi\tau_0)$
$d/h = 24$	0.390	8.15×10^{-3}	0.222
$d/h = 6$	0.395	5.94×10^{-3}	
$d/h = 3$	0.252	6.40×10^{-3}	
$d/h = 2$	0.189	4.98×10^{-3}	0.310
$d/h = 1.33$	0.189	2.38×10^{-3}	0.498
$d/h = 1$	0.097	2.20×10^{-3}	0.546

bifurcation (the same effect was identified by Klotz *et al.* [14]). This imperfect bifurcation can be observed in Fig. 7 in which deviation from a quadratic law can be observed for lower Reynolds numbers. This conclusion is strengthened by the fact that the first supercritical bifurcation is observed in earlier numerical investigations [6–8].

D. Recirculation zone

To estimate the length of the recirculation zone behind the disk, the laser sheet for the PIV measurements of the v_z and v_y components was placed in a plane of symmetry, between two counter-rotating vortices (Fig. 8).

By using the obtained streamlines, it was possible to determine the length of the recirculation zone (Fig. 9). In the case of the unsteady regime, with hairpin shedding, results were averaged over an integer number of oscillation periods (red circles). In addition, the maximum and minimum length of the recirculation zone (black squares and magenta triangles respectively) was calculated. The present results were obtained in experiments with a disk having $d/h = 1.33$.

In the steady axisymmetric and steady asymmetric regimes, the length of the recirculation zone increases nearly linearly with the Reynolds number. In the regime of an unsteady flow with hairpin shedding, the recirculation length decreases with growing Re . The same behavior was observed by Zielińska *et al.* [15] for the flow behind a circular cylinder, for which the mean flow modification (zero mode) from nonlinearities is described at the origin of this stretching. However, our results clearly show that the stationary streamwise vortex makes negligible contribution to this mean flow modification. Similar results were observed in direct numerical simulation (DNS) of flow behind spheres by Bouchet *et al.* [16]. In addition, we observed that the contribution of the hairpin to this nonlinear effect is weak, as compared to similar effects for the flow behind a cylinder.

Further work is planned to characterize the azimuthal vorticity $\omega_{\theta \max}$ inside the recirculation loop and thus to compare it with the criteria of Ref. [17] to predict the regular transition when $\omega_{\theta \max}/(2U/d)$ reaches an onset. This onset is expected to weakly depend on the Reynolds number.

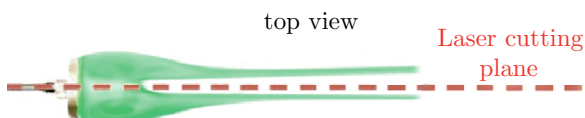


FIG. 8. (Color online) Placement of cutting laser plane.

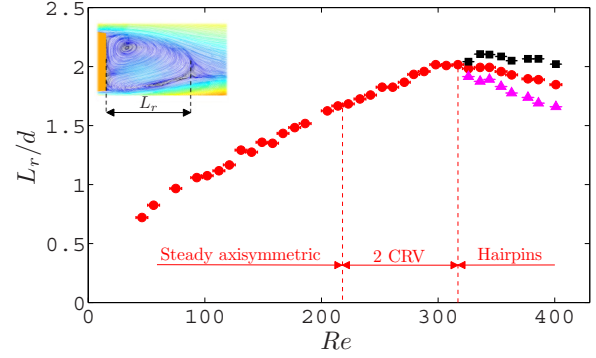


FIG. 9. (Color online) Length of the recirculation zone L_r as a function of Reynolds number ($d/h = 1.33$). In the inset, it is possible to observe the nonsymmetric recirculation zone. Red circles, black squares, and magenta triangles denote average, maximum, and minimum length L_r of the recirculation zone, respectively.

IV. DATA ANALYSIS—AZIMUTHAL FOURIER DECOMPOSITION

A. Spatial analysis

To characterize in detail the evolution of main features of the flow with the growing Re , we performed an azimuthal Fourier decomposition of the longitudinal vorticity field. This field was obtained through PIV measurements at $z = 1.25d$ (see also Ref. [18]). In the first step axial vorticity ω_z is interpolated from a Cartesian to a polar grid, providing ω_z for a discrete set of radii r_j and angles θ_n . In the second step a sequence of one-dimensional azimuthal Fourier transforms is evaluated

$$\hat{\omega}^{\text{azim}}(r_j, m) = \sum_n \omega_z(r_j, \theta_n) \exp(-im\theta_n), \quad (1)$$

and subsequently integrated in the radial direction:

$$\hat{\omega}_m = \sum_j \hat{\omega}^{\text{azim}}(r_j, m) r_j \delta r, \quad (2)$$

yielding the azimuthal modal coefficients of the longitudinal vorticity.

B. Mode patterns

Examples of this decomposition for an instantaneous field of the axial vorticity are shown in Figs. 10 and 11. The patterns of the first four main polar modes are presented for two different flow regimes: the regime with two stationary counter-rotating vortices in the wake (Fig. 10) and the unsteady regime with hairpin shedding (Fig. 11). As the flow preserves planar symmetry, it is not surprising that the mode $m = 1$ contains most of the flow energy and resembles with satisfactory accuracy the full PIV streamwise vorticity image.

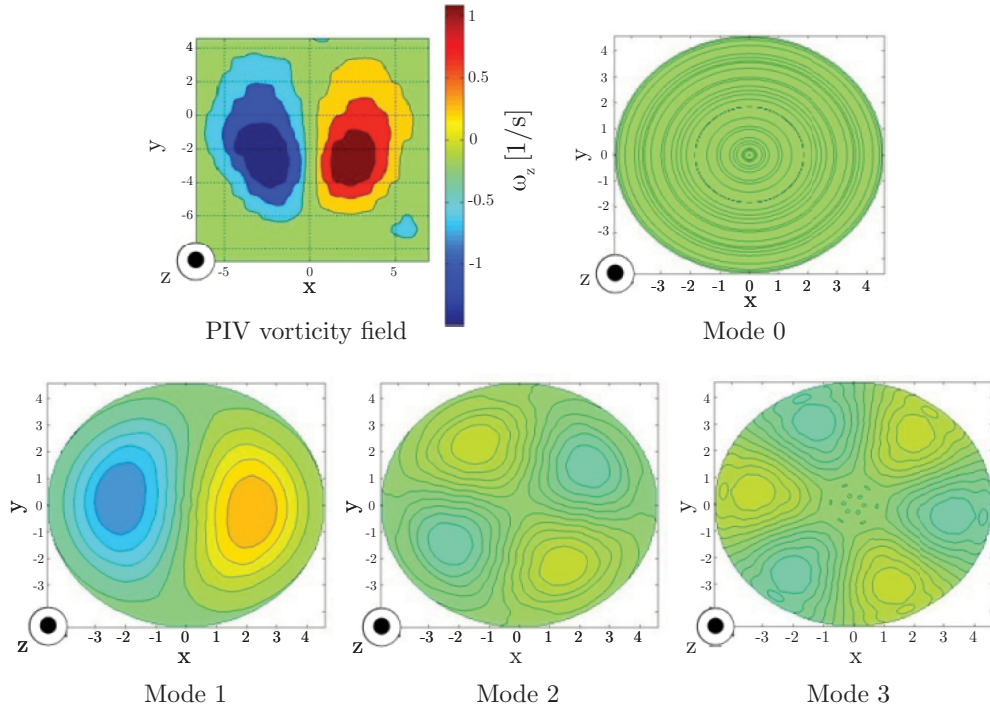


FIG. 10. (Color online) PIV vorticity field and mode patterns in the regime with two steady counter-rotating vortices ($d/h = 2$, $Re = 239$).

The same observation can be made for flows with hairpin shedding. Again the pattern of the mode $m = 1$ is very similar to the original PIV image as the hairpin shedding preserves the plane symmetry for the range of Reynolds numbers that we have explored.

C. Time evolution of mode energy and vortex shedding frequency

The energy of different azimuthal modes (Fig. 12) was determined as a function of time for a fixed Reynolds number. The mode $m = 1$ makes the strongest contribution to the flow

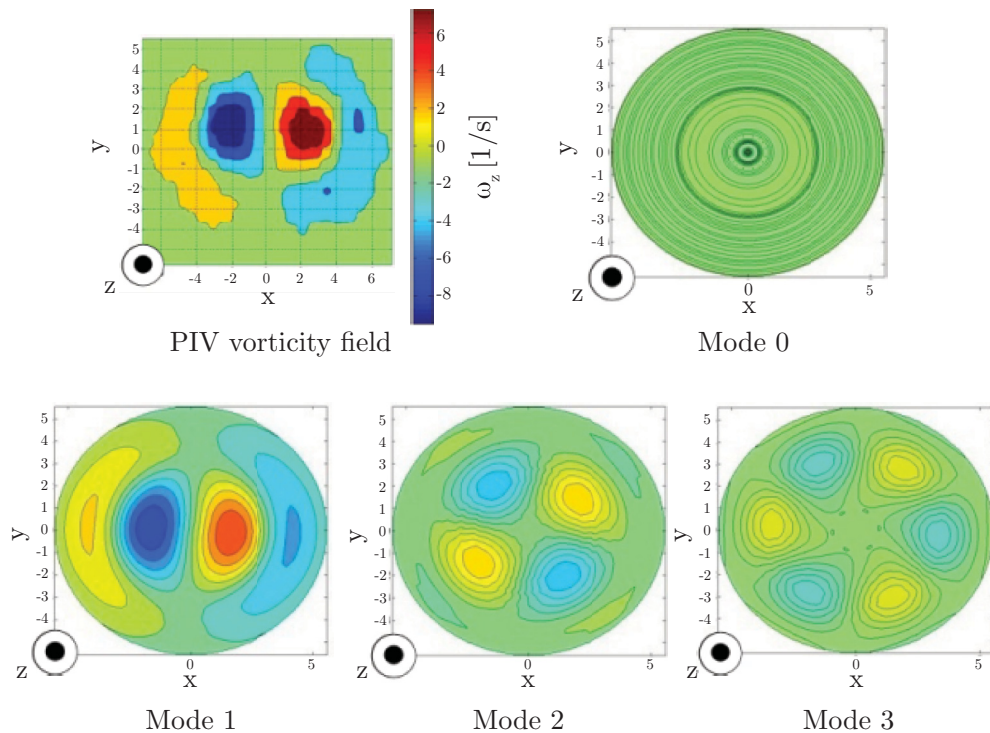


FIG. 11. (Color online) PIV vorticity field and mode patterns in the regime of hairpin shedding ($d/h = 2$, $Re = 303$).

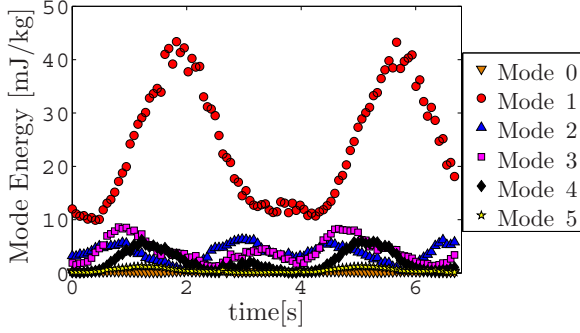


FIG. 12. (Color online) Time evolution of energy of first five azimuthal modes in the regime of hairpin shedding ($d/h = 24$, $Re = 204$).

containing most of the flow energy as the system preserves a planar symmetry. Other higher modes are also displayed. The analysis was concentrated on the first five modes ($m = 0, 1, 2, 3$, and 4), which contain most of the energy and are physically significant. It can be observed that modes 2, 3, and 4 have higher frequency f (smaller period). The experimental results indicate that the frequency of higher modes can be expressed as $f_m = mf_1$.

The increased longitudinal vorticity with the hairpin shedding regime arises from the periodic contribution of the legs of these coherent structures. We can suppose that the variation in ω_z , observed for the mode $m = 1$ in Fig. 12, can be explained as follows: When the legs are nearly horizontal, they contribute the maximum energy to the longitudinal ω_z , while the minimum corresponds to the moment when the vorticity is almost transversal, to the plane of measurement as the head of the hairpin crosses this plane. The increase in longitudinal vorticity comes from the superposition of the unsteady leg vorticity and the steady counter-rotating vortex, which are issues of regular bifurcation.

We study how the frequency, in the unsteady regime with hairpin shedding, changes with Reynolds number and determine the influence of the disk aspect ratio on this parameter.

For each time sequence of the velocity field, the period of hairpin shedding was determined by measuring the time interval between maxima present in the signal. The estimated frequency depends linearly on Reynolds number (Fig. 13). Equation (3) describes the best fit for the case of the disk with

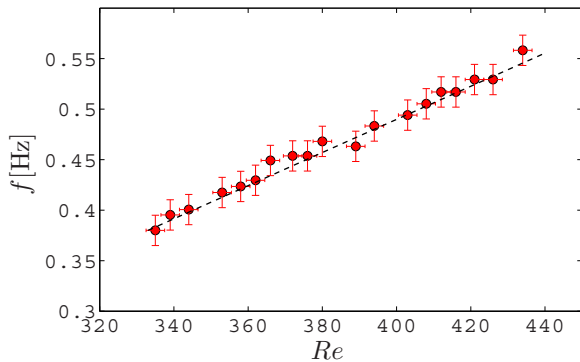


FIG. 13. (Color online) Hairpin shedding frequency as a function of Re for $d/h = 1$.

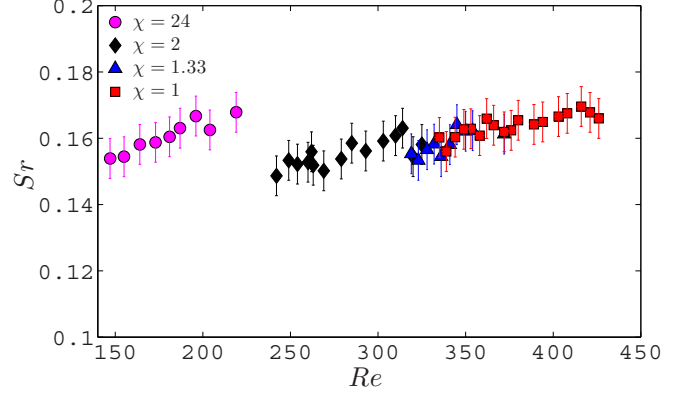


FIG. 14. (Color online) Strouhal number of hairpin shedding as a function of Re , for different values of aspect ratio χ of the disk.

$d/h = 1$:

$$f = 0.38 + 16 \times 10^{-4}(Re - 333)[s^{-1}]. \quad (3)$$

The initial Strouhal number Sr (where $Sr = \frac{fd}{U}$) obtained when the Reynolds number is close to Re_{c2} , is 0.15 for the investigated disks with $d/h = (1, 1.33, 2, 24)$ (Fig. 14).

D. Mode energy bifurcations

It was also determined how the maximum energy of different modes changes with the Reynolds number. The maximum energy was defined as the maximum energy present in the signal of a particular mode. Three different aspect ratios were analyzed: $d/h = 24$ (Fig. 15), $d/h = 1.33$ (Fig. 16), and $d/h = 1$ (Fig. 17).

For all disks, the greatest change in the mode behavior was observed during the transition to the unsteady regime. However, for the disk with $d/h = 1$, the mode 1 for $310 < Re < 333$ grows slower than for $Re > 333$. The same phenomenon observed by Gumowski *et al.* [11] was described as an unsteady regime with peristaltic oscillations. The identical behavior is observed in the case of the disk with $d/h = 1.33$, but the range (ΔRe) of this regime is shorter. This phenomenon is not observed at larger aspect ratios.

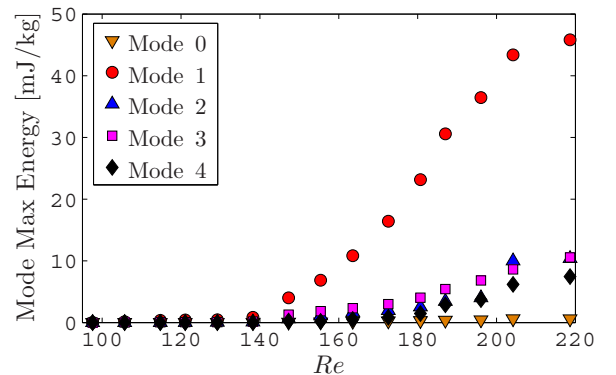


FIG. 15. (Color online) Mode energy bifurcation curve for $d/h = 24$.

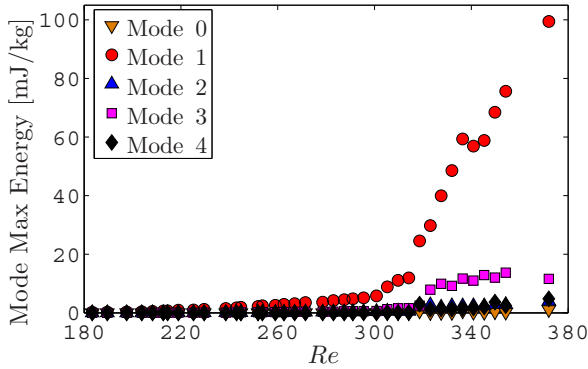


FIG. 16. (Color online) Mode energy bifurcation curve for $d/h = 1.33$.

V. COMPARISON WITH NUMERICAL SIMULATIONS

The growing possibilities of computational fluid dynamics have recently allowed the analysis of the wake instability in a flow around the disk ([6–8,19]) by employing 3D Navier–Stokes simulations. These works have reported the stationary axisymmetric regime as well as the stationary nonaxisymmetric regime followed by a regime of vortex shedding in which the symmetry plane either rotates in time [6] or kinks [8] or, alternatively, a shifted hairpin shedding occurs [7]. This latter regime has a very short range ΔRe between 5 and 10, as observed in Refs. [6–8,19]. It depends on the aspect ratio and is followed by an unsteady hairpin shedding regime characterized by a fixed plane of symmetry. Despite the narrow range of Reynolds numbers, which is difficult to observe in the experiment, we do not observe this behavior, perhaps due to the (mentioned earlier) influence of disturbances produced by the disk support system.

One of the disks that we have investigated experimentally had $d/h = 3$. Because the same disk was analyzed in Ref. [6], it is worth comparing the results.

The bifurcation curve for the disk with $d/h = 3$ is presented in Fig. 18. The first transition was observed for $Re_{c1} = 142$, while the numerical prediction indicates $Re_{c1} = 160$. The second onset, which corresponds to a transition to unsteady flow with hairpin shedding, was experimentally observed

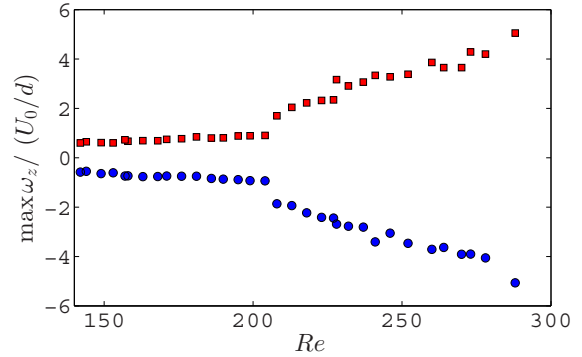


FIG. 18. (Color online) Vorticity bifurcation curve for $d/h = 3$.

for $Re_{c2} = 202$, while Ref. [6] predicted this transition at $Re_{c2} = 180$.¹

The initial Strouhal number, for each analyzed disk, remained close to 0.15, which exceeds the numerical predictions by over 30%. Auguste *et al.* [6] obtained $Sr = 0.11$ for a disk with $d/h = 3$, and Shenoy and Kleinstreuer [8] obtained $Sr = 0.113$ for a disk with $d/h = 10$.

The influence of the disk aspect ratio was studied by Fernandes *et al.* [20]. The dependence of the first onset as a function of the disk aspect ratio was determined as $Re_{c1}(d/h) = 116.5[1 + (d/h)^{-1}]$. Experimentally, we obtained the relation $Re_{c1}(d/h) = 115[1 + (d/h)^{-1}]$. However, the results concerning the second onset are less consistent with the predictions of Fernandes *et al.* In the case of the thickest disk, the extension of the second regime range is almost five times what numerical prediction indicates.

In addition, we determined that another bifurcation can be observed for thicker disks. It leads to unsteady flow with peristaltic small oscillations of the two longitudinal vortices. This kind of wake behavior has previously not been obtained numerically.

VI. CONCLUSIONS

This paper presents detailed measurements of the velocity field around disks having different aspect ratios. From these data, we were able to obtain well-defined values for the onset of the successive bifurcations occurring in this flow. First, we showed that the stronger shear developing in the thinner disk first destabilizes the stationary axisymmetric (a lower aspect ratio corresponds to a higher critical Reynolds number) recirculation region behind the disk, then destroys the homogeneous toroidal shape, producing a deformed torus with a varying, near-circular cross section. Simultaneously, two threads of longitudinal vorticity are generated in the small recirculation zone. The same behavior was observed for the onset of the unsteady second instability, with vortex (hairpin) shedding from one side of the disk. In addition, we observed

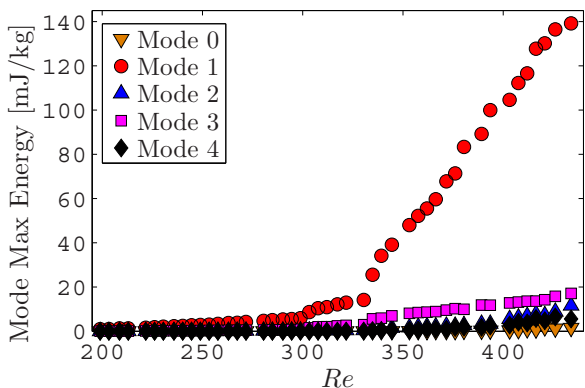


FIG. 17. (Color online) Mode energy bifurcation curve for $d/h = 1$.

¹They observed, in the Reynolds interval [184, 215], four different nonstationary regimes with broken reflectional symmetry, before the recovery of oscillations in a fixed plane, as we observed experimentally.

that the range between these two onsets increases when the aspect ratio reduces, opening the possibility to explore in greater detail the interesting region of peristaltic fluctuations that we discovered earlier in the case of flow around spheres [11]. For the first time the experiments allowed us to obtain the values of the Landau coefficients for different disk aspect ratios. These values were obtained both for the first stationary instability as well as for the unsteady Hopf bifurcation. For this, we give also the laws of the nonlinear variation in the frequency with the Reynolds number. We can fully describe nonlinearities in terms of Landau coefficients, if the complex amplitude equations are written as

$$\tau_0 \frac{dA}{dt} = \epsilon_0(1 + ic_0)A - g(1 + ic_2)|A|^2A, \quad (4)$$

where $A = \rho e^{i\varphi}$, ρ stands for the maximum of the order parameter, while ω_f and $\frac{d\varphi}{dt}$ denote the frequency and its nonlinear increase at the onset. This model seems to compare

well with the Eq. (3), in which

$$f = f_0 + \frac{c_0 - c_2}{2\pi\tau_0\text{Re}_{c_2}}(\text{Re} - \text{Re}_{c_2}).$$

One of the most important results obtained in this paper is the confirmation of the increase in longitudinal streamwise vorticity observed in the hairpin shedding regime, as observed in Fig. 12. Indeed, this value varies between a maximum, which is the contribution of the legs of the hairpins, and a minimum, which is the extrapolated value of the stationary streamwise vorticity of the regular steady regime. We earlier observed the same behavior in the case of a wake around a sphere [11] as well as a cube [14], and this behavior seems to be a universal trend for the wake instability reported also by other authors for 3D bodies such as oblate spheroids [21], elongated finite cylinders [22], and jets in crossflows [23].

ACKNOWLEDGMENTS

We acknowledge M. Chrust and L. Tuckerman for help in modal analysis, P. Jenffer for technical assistance, and J. Rokicki for discussions.

-
- [1] M. Kiya, H. Ishikawa, and H. Sakamoto, *J. Wind Eng. Id. Aerod.* **89**, 1219 (2001).
 - [2] D. Marshall and T. E. Stanton, *Proc. R. Soc. London, Ser. A* **130**, 295 (1931).
 - [3] F. Ross and W. Willmarth, *AIAA J.* **9**, 285 (1971).
 - [4] S. Cannon, F. Champagne, and A. Glezer, *Exp. Fluids* **14**, 447 (1993).
 - [5] E. Berger, D. Scholz, and M. Schumm, *J. Fluids Struct.* **4**, 231 (1990).
 - [6] F. Auguste, D. Fabre, and J. Magnaudet, *Theor. Comput. Fluid Dyn.* **24**, 305 (2010).
 - [7] P. Meliga, J. Chomaz, and D. Sipp, *J. Fluid Mech.* **633**, 159 (2009).
 - [8] A. R. Shenoy and C. Kleinstreuer, *J. Fluid Mech.* **605**, 253 (2008).
 - [9] E. Lazar, B. DeBlauw, N. Glumac, C. Dutton, and G. Elliott, in *27th AIAA Aerodynamic Measurement Technology and Ground Testing Conference, Chicago, Illinois* (AIAA, Reston, VA, 2010), p. 4355.
 - [10] L. Lourenco and A. Krothapalli, *Exp. Fluids* **18**, 421 (1995).
 - [11] K. Gumowski, J. Miedzik, S. Goujon-Durand, P. Jenffer, and J. E. Wesfreid, *Phys. Rev. E* **77**, 055308 (2008).
 - [12] A. Roshko, On the Drag and Shedding Frequency of Two-dimensional Bluff Bodies, NACA Technical Note 3169 (1954).
 - [13] M. Chrust, Ph.D. thesis, University of Strasbourg-France, 2012.
 - [14] L. Klotz, S. Goujon-Durand, J. Rokicki, and J. Wesfreid, *J. Fluid Mech.* 2014 (to be published).
 - [15] B. J. A. Zielinska, S. Goujon-Durand, J. Dusek, and J. E. Wesfreid, *Phys. Rev. Lett.* **79**, 3893 (1997).
 - [16] G. Bouchet, M. Mebarek, and J. Dusek, *Eur. J. Mech. B* **25**, 321 (2006).
 - [17] J. Magnaudet and G. Mougin, *J. Fluid Mech.* **572**, 311 (2007).
 - [18] P. Szaltys, M. Chrust, A. Prządka, S. Goujon-Durand, L. S. Tuckerman, and J. E. Wesfreid, *J. Fluids Struct.* **28**, 483 (2012).
 - [19] D. Fabre, F. Auguste, and J. Magnaudet, *Phys. Fluids* **20**, 051702 (2008).
 - [20] P. Fernandes, F. Risso, P. Ern, and J. Magnaudet, *J. Fluid Mech.* **573**, 479 (2007).
 - [21] M. Chrust, G. Bouchet, and J. Dusek, *J. Fluid Mech.* **665**, 199 (2010).
 - [22] P. Bohorquez, E. Sanmiguel-Rojas, A. Sevilla, J. I. Jimenez-Gonzalez, and C. Martinez-Bazan, *J. Fluid Mech.* **676**, 110 (2011).
 - [23] M. Ilak, P. Schlatter, S. Bagheri, and D. Henningson, *J. Fluid Mech.* **696**, 94 (2012).